




# Int&in: A machine learning-based web server for active split site identification in inteins

Mirko Schmitz<sup>1,2,4</sup>  | Jara Ballestin Ballestin<sup>1,2,5</sup> | Junsheng Liang<sup>1,2</sup> |  
 Franziska Tomas<sup>1,2,6</sup> | Leon Freist<sup>3</sup> | Karsten Voigt<sup>3</sup> |  
 Barbara Di Ventura<sup>1,2</sup>  | Mehmet Ali Öztürk<sup>1,2</sup> 

<sup>1</sup>BIOSS and CIBSS Research Signalling Centers, University of Freiburg, Freiburg, Germany

<sup>2</sup>Institute of Biology II, University of Freiburg, Freiburg, Germany

<sup>3</sup>Institute of Biology III, University of Freiburg, Freiburg, Germany

<sup>4</sup>4HF Biotech GmbH, Freiburg, Germany

<sup>5</sup>Bioprocess Innovation Unit, ViraTherapeutics GmbH, Rum, Austria

<sup>6</sup>Department of Molecular Life Sciences, University of Zurich, Zurich, Switzerland

## Correspondence

Barbara Di Ventura and Mehmet Ali Öztürk, BIOSS and CIBSS Research Signalling Centers, University of Freiburg, Freiburg, Germany.

Email: [barbara.diventura@bio.uni-freiburg.de](mailto:barbara.diventura@bio.uni-freiburg.de); [mehmet.oeztuerk@bioss.uni-freiburg.de](mailto:mehmet.oeztuerk@bioss.uni-freiburg.de)

## Funding information

Deutsche Forschungsgemeinschaft, Grant/Award Number: 422681845; Horizon 2020 Framework Programme, Grant/Award Number: 101002044

**Review Editor:** Nir Ben-Tal

## Abstract

Inteins are proteins that excise themselves out of host proteins and ligate the flanking polypeptides in an auto-catalytic process called protein splicing. In nature, inteins are either contiguous or split. In the case of split inteins, the two fragments must first form a complex for the splicing to occur. Contiguous inteins have previously been artificially split in two fragments because split inteins allow for distinct applications than contiguous ones. Even naturally split inteins have been split at unnatural split sites to obtain fragments with reduced affinity for one another, which are useful to create conditional inteins or to study protein–protein interactions. So far, split sites in inteins have been heuristically identified. We developed Int&in, a web server freely available for academic research (<https://intein.biologie.uni-freiburg.de>) that runs a machine learning model using logistic regression to predict active and inactive split sites in inteins with high accuracy. The model was trained on a dataset of 126 split sites generated using the gp41-1, *Npu* DnaE and CL inteins and validated using 97 split sites extracted from the literature. Despite the limited data size, the model, which uses various protein structural features, as well as sequence conservation information, achieves an accuracy of 0.79 and 0.78 for the training and testing sets, respectively. We envision Int&in will facilitate the engineering of novel split inteins for applications in synthetic and cell biology.

## KEYWORDS

Aes, CL intein, gp41-1, machine learning, *Npu* DnaE, protein engineering, split inteins, split site prediction

## 1 | INTRODUCTION

Inteins are small intervening proteins translated within host proteins that perform a so-called protein splicing reaction to excise themselves out of their flanking

external polypeptides (exteins), which are ligated through a new peptide bond (Di Ventura & Mootz, 2019). Alongside contiguous inteins, which originate from a single gene (Figure 1a), split inteins (Figure 1b) encoded by two separate genes are of particular interest because they

This is an open access article under the terms of the [Creative Commons Attribution-NonCommercial](https://creativecommons.org/licenses/by-nc/4.0/) License, which permits use, distribution and reproduction in any medium, provided the original work is properly cited and is not used for commercial purposes.

© 2024 The Authors. *Protein Science* published by Wiley Periodicals LLC on behalf of The Protein Society.

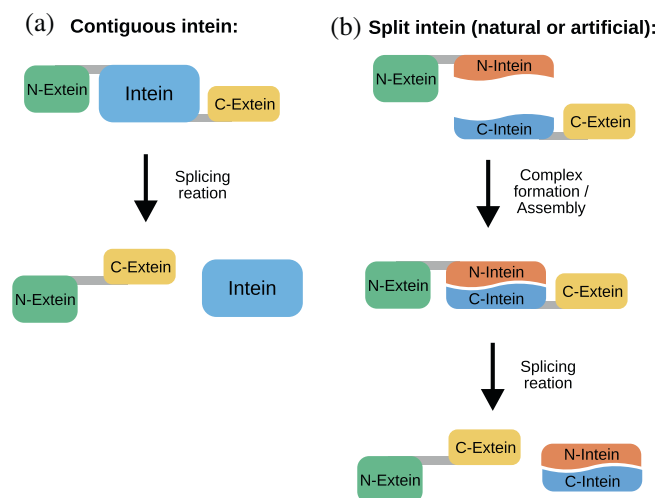


**FIGURE 1** Schematic representation of the protein splicing reaction carried out by contiguous (a) and split (b) inteins.

allow for a greater variety of applications (Waldhauer et al., 2015; Pan et al., 2016; Ye et al., 2018; Villiger et al., 2018; Lopez-Igual et al., 2019; Palei et al., 2019; Wang et al., 2019; Palanisamy et al., 2019; Purde et al., 2020; Choi et al., 2021). In the *trans*-splicing reaction, the N-terminal intein fragment (the ‘N-intein’) must first form a complex with the C-terminal intein fragment (the ‘C-intein’). After this step, the splicing reaction takes place resulting in the fusion of the N- and C-exteins (Figure 1b). In the past, inteins have been artificially split to obtain either a split intein out of a contiguous one (Mootz & Muir, 2002; Brenzel et al., 2006) or two intein fragments with low affinity for each other that could be induced to splice when in close physical proximity (Mootz & Muir, 2002; Tyszkiewicz & Muir, 2008; Yao et al., 2020). By controlling the physical proximity of the intein fragments with an external trigger such as light (Tyszkiewicz & Muir, 2008) or a chemical (Mootz & Muir, 2002), protein splicing is achieved in a conditional way, allowing interesting applications in synthetic and chemical biology (Mootz et al., 2003; Wong et al., 2015; Böcker et al., 2019) and cell biology (Lee & Muir, 2023). Alternatively, the intein fragments can be fused to proteins whose interaction one wishes to determine. If the proteins interact, splicing occurs leading to the accumulation of a splice product, such as a fluorescent protein, which can be easily quantified and is stable over time unless otherwise engineered (Yao et al., 2020). We call a split site allowing the splicing reaction to occur *active*, while one corresponding to two intein fragments unable to splice *inactive*.

So far, active split sites in inteins have been found with heuristic approaches (Wu et al., 1998; Mootz & Muir, 2002), or taking very simple protein structure

considerations into account (Otomo et al., 1999). The existing SPELL algorithm (<https://dokhlab.med.psu.edu/spell/>) that was developed to computationally predict split sites in proteins for the construction of chemogenetic and optogenetic split proteins (Dagliyan et al., 2018), is inadequate for the specific case of inteins: we found that for ~80% of inteins collected from the literature (Aranko et al., 2014) no split sites could be predicted (33 inteins without any predicted split sites versus 8 with predicted sites (3D structures were predicted with AlphaFold2 (Jumper et al., 2021) as implemented in ColabFold (Mirdita et al., 2022); *Source Data*, File S1)). Moreover, for the split sites predicted to be active by SPELL, one site was experimentally shown to be active, while another to be inactive (Table S1). A different recently reported computational approach, ProteinSplit (<http://elixir.fkkt.um.si/ProteinSplitIndex.html>), is tailor-made for the prediction of ligand-mediated protein dimerization (Rihtar et al., 2023), and therefore unsuitable for the purposes of predicting active split sites in inteins. The ability to identify new active split sites in any intein of choice in an easy and confident manner would represent a breakthrough in the field and encourage a wider range of intein-based applications.

Here we apply machine learning (ML) to create an algorithm to predict active split sites in inteins. ML is a branch of artificial intelligence aiming to design algorithms that learn to recognize patterns in input datasets and make useful predictions on data not seen before. Given their power, ML algorithms started to pervade almost any research field, including molecular biology. ML approaches can be grouped into 4 different categories (Jovel & Greiner, 2021; Kouba et al., 2023): (1) supervised learning; (2) unsupervised learning; (3) semi-supervised learning; and (4) reinforcement learning. In supervised learning, models are trained on labeled data, where the connection between input and correct output is manually done to allow the algorithm to learn the connection and apply it later on a new, unlabeled dataset. Unsupervised learning models find hidden patterns or intrinsic structures in unlabeled input data. These models are particularly useful if labeled data are unavailable or too costly to obtain. In semi-supervised learning, the training data consist of a combination of labeled and unlabeled data. Reinforcement learning is a type of machine learning paradigm where the program learns to make sequential decisions to maximize cumulative rewards. The selection of the ML algorithm depends on diverse factors. If labeling data is a possibility, and the task is not about finding anomalies or reducing the dimensionality, then supervised learning is a natural choice. Lately, many ML algorithms have been put forward in the field of structural biology and protein design using a variety of learning

methods (Khurana et al., 2018; Wang et al., 2019, 2023; Ferruz et al., 2022; Watson et al., 2023). Further information about the methodology, pitfalls and outlook of ML applications in protein engineering can be found in recent reviews (Villalobos-Alva et al., 2022; Kouba et al., 2023; Khakzad et al., 2023).

We used supervised learning to create an algorithm that combines several sequence and structural features, global or local in respect to the split site, and applies a logistic regression classification method on these features to predict the likelihood that a split site will be active. It moreover shows separation power with regard to the splicing efficiency, meaning it can be used to distinguish split sites that lead to fragments that reassemble efficiently and those that do not. The latter ones are particularly valuable for the creation of novel conditional split inteins. We validate the algorithm using data taken from the literature as well as generated by us and show that it has an accuracy of 0.79 for the training set and 0.78 for the testing dataset. The algorithm is freely available for academic research on the Int&in web server (<https://intein.biologie.uni-freiburg.de/>), while the source code of a standalone program is available on Github (<https://github.com/bleblebles/Int-In/>).

## 2 | RESULTS

### 2.1 | Creation of a dataset of active and inactive split sites in inteins

To train the machine learning model, we needed unbiased information not only on active sites—which are easily retrievable from the literature, but also on inactive ones. Therefore, we decided to generate a dataset of split sites using three inteins: gp41-1 (Carvajal-Vallejos et al., 2012), *Npu* DnaE (Iwai et al., 2006) and CL (a cysteine-less intein) (Bhagawati et al., 2019). To cover the whole sequence space of each intein, we randomly selected split sites to be experimentally tested with the only rule being that intein fragments had to be at least four residues long, because we reasoned that three or less residues would unlikely reassemble with the cognate fragment (Appleby et al., 2009; Mootz, 2009). The split sites were experimentally tested using Western blots as readout with antibodies allowing for the detection of the constructs made of the N-extein and the N-intein (N-construct), the C-intein and the C-extein (C-construct), as well as the splice product (Figure 2a,b, Source Data, File S2). As exteins we selected proteins known to be soluble in *Escherichia coli*: the maltose binding protein (MBP; N-extein), and thioredoxin (TRX) and SUMO with a FLAG tag (fused together; C-extein). To maximize the

splicing reaction, we added the so-called “local exteins” (3–5 amino acids preceding the N-intein and 3–5 following the C-intein) (Lockless & Muir, 2009; Carvajal-Vallejos et al., 2012; Stevens et al., 2017; Bhagawati et al., 2019). These were separated from the exteins with a flexible linker (Figure 2c). We tested a total of 126 split sites (36 for gp41-1, 44 for *Npu* DnaE and 46 for CL) (Figure 2d). We considered active a site for which a band, albeit faint, could be detected at the size of the splice product. Of the 126 tested split sites, 64 were found to be inactive, and 62 to be active (Figure 2d). Efficiency of splicing varied across the split sites (Figure S1, and Source Data, File S3). Notably, inteins split at unnatural sites might exhibit a higher propensity for N- and/or C-cleavage, which are side-reactions of the main splicing reaction (Shah & Muir, 2013). Our design makes it difficult to assess this quantitatively, because the difference in size between the N-construct and the N-extein (i.e., the potential product of a N-cleavage) as well as between the C-construct and the C-extein (i.e., the potential product of a C-cleavage) is too small to be detected on a Western blot for many split sites. A different approach should be adopted to specifically account for N- and C-cleavage. Nonetheless, our calculations of splicing efficiencies at least indirectly reflect the presence of such side-reactions, which compete with the main splicing reaction and therefore inevitably lead to less splice product. We tried to indicate the presence of these side reactions as best as possible for split sites where the size difference allowed us to distinguish their products from the precursors (Figure S1).

### 2.2 | Finding structural and biochemical properties with predictive power

Next, we sought to find evolutionary, structural and biochemical properties within inteins that may be helpful in discriminating between active and inactive split sites. These properties were extracted from the inteins' sequences and structures (for gp41-1 and *Npu* DnaE, crystal structures (PDB id: 6QAZ and PDB id: 4KL5, respectively), while for CL a structure generated through the ColabFold implementation (Mirdita et al., 2022) of AlphaFold2 (Jumper et al., 2021); Source Data, File S4). We considered the following properties: (i) binding affinity between the two resulting intein fragments, given its strong influence on whether a complex is formed or not (Figure 3a) (Vangone & Bonvin 2015, 2017); (ii) conservation of the residues around the split site (either based solely on sequence or based on spatial proximity in the 3D structure), as conserved regions are typically structurally or functionally important and should

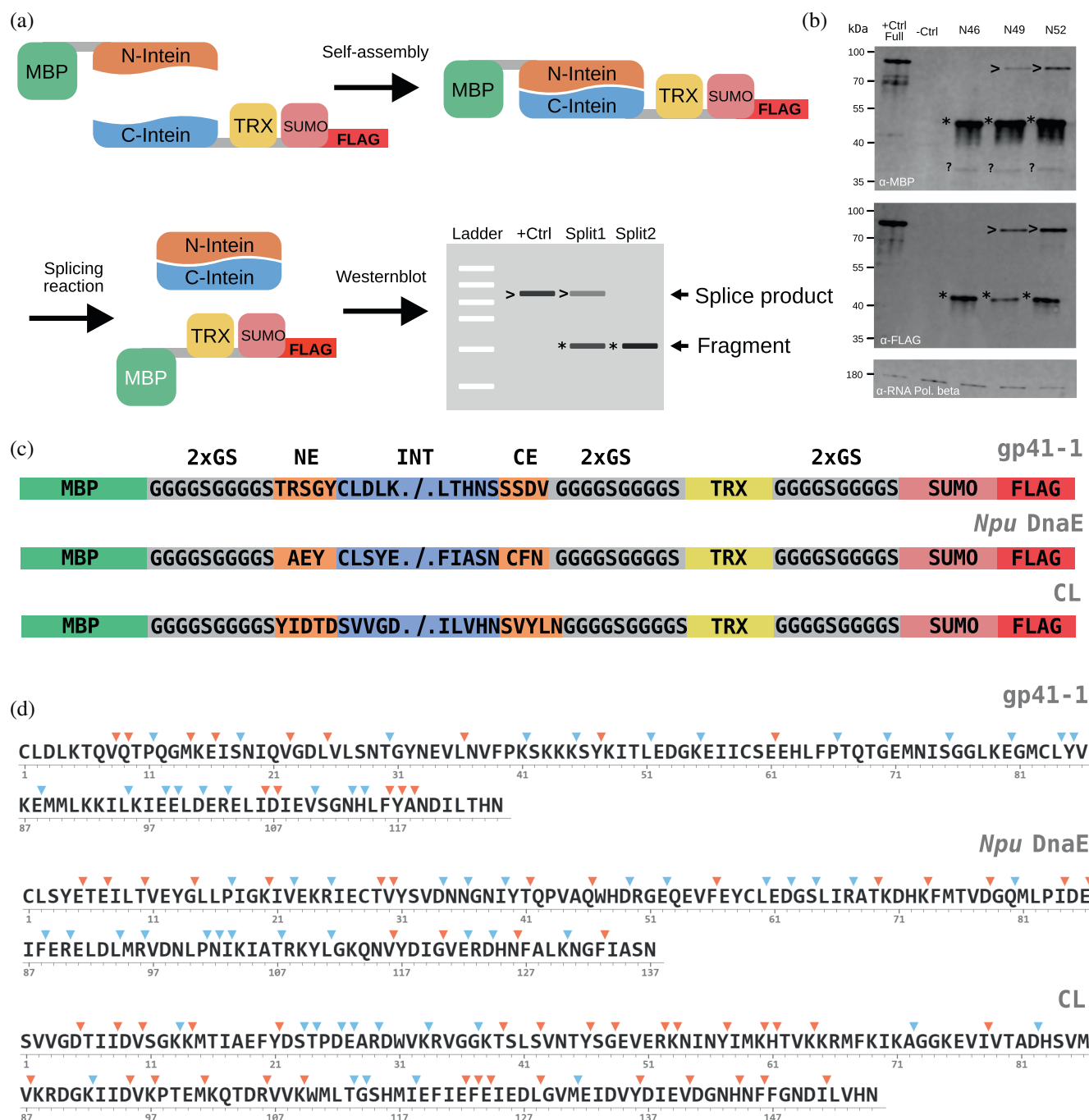


**FIGURE 2** Generation of the dataset of split inteins for the development of the algorithm used in the Int&in web server. (a) Schematic representation of the experimental setup. MBP, maltose binding protein. TRX, thioredoxin. +Ctrl, positive control consisting of the MBP-TRX-SUMO-FLAG fusion protein, additionally having the gp41-1 local exteins between MBP and TRX. Split1, Split2, examples of split sites that will be analyzed. (b) Exemplary Western blot showing the splicing activity of *Npu DnaE* split at the indicated sites. NX, intein split at the amino acid at position X from the first amino acid of the intein (the N-terminus). +Ctrl Full, positive control consisting of the full-length intein, artificially expressed as contiguous intein. -Ctrl, negative control consisting of untransformed cells. \*, precursor (N-intein visualized with the anti-MBP antibody, or C-intein visualized with anti-FLAG antibody). >, splice product.?, likely degradation product. Loading control, RNA polymerase beta-subunit. The N-extein (MBP) is approximately 42 kDa. The C-extein (TRX-SUMO-FLAG) fusion protein is expected to be around 26 kDa. The longest gp41-1 fragment is expected to be about 13 kDa. Thus, the N-/C-inteins (N-intein: MBP + N-terminal intein fragment; C-intein: C-terminal intein fragment + TRX-SUMO-FLAG) are expected to be maximally 55 and 39 kDa respectively. The local exteins are expected to contribute minimally to the final size of the proteins. Notably, the splice product and the C-constructs run at a higher molecular weight than expected. (c) Schematic representation of the construct design for gp41-1, *Npu DnaE* and CL inteins split at various sites. The “split cassette” used to create the split versions is not visualized for simplicity. See Materials and Methods for details. NE, N-terminal local exteins. CE, C-terminal local exteins. (d) Sequences of the inteins used to generate the dataset and location of split sites. The color code indicates active (cyan) and inactive (orange) sites as experimentally assessed via Western blot. The numbers indicate residue positions.



better not be tampered with (Figure 3a); (iii) relative surface accessibility of the residues around the split site, considering that residues exposed on the protein surface are likely to contribute less to overall protein stability than those residing in the core, and might thus be a good predictor for active split sites (Figure 3a); (iv) secondary structure elements, as regions with loops may contribute less to protein structure and could be favorable to locate split sites (Figure 3a); (v) affinity between the the first  $n$  residues of the C-intein and the full N-intein (what we call C-fragment docking) (Figure 3a). We considered this property having in mind the ‘capture and collapse’

mechanism introduced by Shah and colleagues, who investigated the naturally split *Npu* DnaE intein through NMR (Shah et al., 2013). The partially folded N-intein binds to the unfolded C-intein in a process termed *capture*, leading to an intermediate structure formed by the fully folded N-intein electrostatically bound by the still unfolded C-intein. During the *collapse* step, the C-intein folds, generating the functional split intein complex. Assuming generalizability of this mechanism, we decided to consider the C-fragment docking energy as a measure of how easily the intermediate structure of the intein forms.

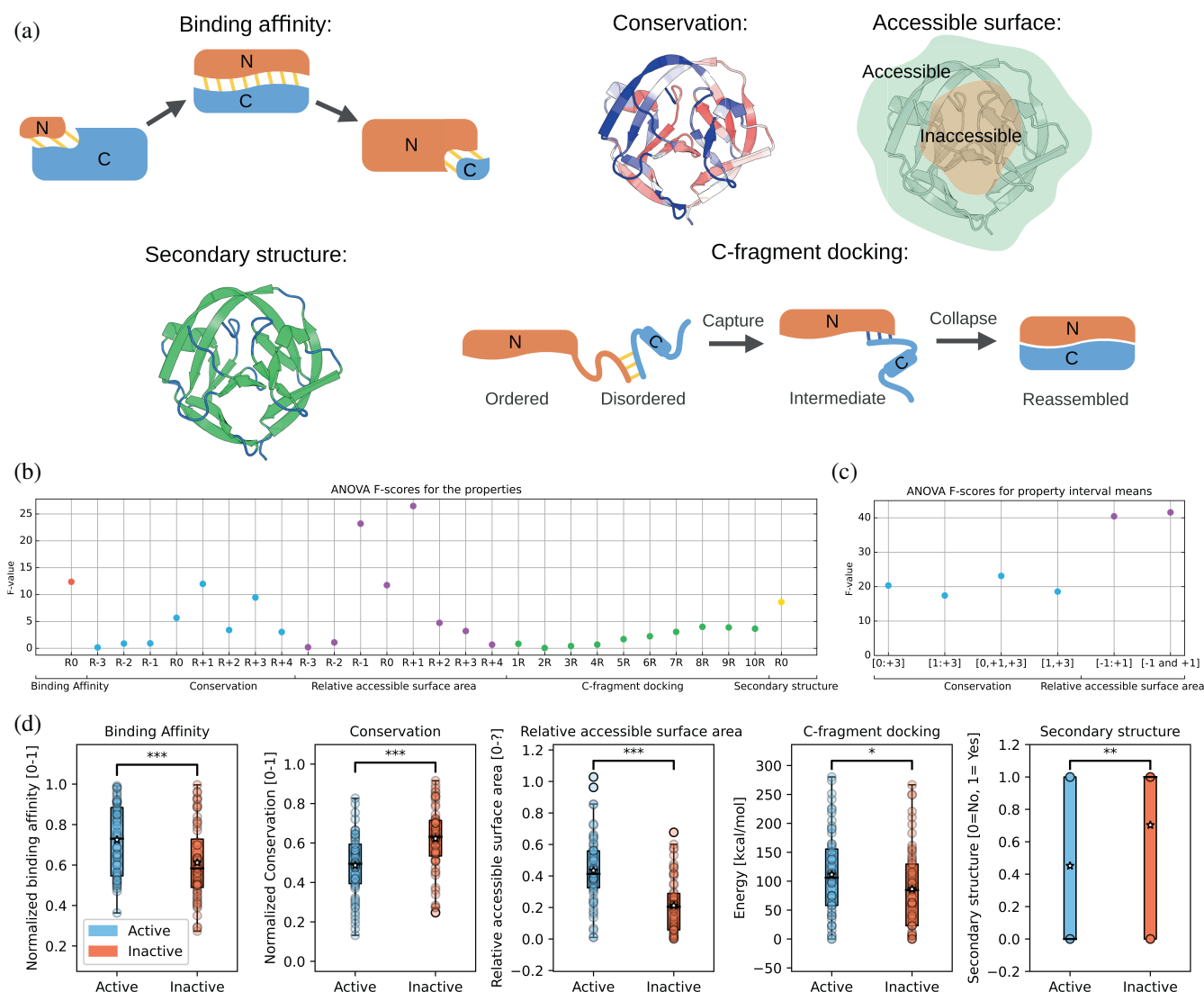


**FIGURE 3** Protein sequence and structure properties with predictive power for discriminating between active and inactive split sites in inteins. (a) Depictions of the binding affinity, conservation (conserved residues are shown in red and non-conserved residues in blue), secondary structure (helices and beta sheets are shown in green and unstructured elements in blue), C-fragment docking (binding energy of the last 10 amino acids of the C-fragment to the N-fragment) are shown. (b) ANOVA  $F$ -scores for the different properties. (c) ANOVA  $F$ -scores for the mean of several sums of residues' properties for conservation and relative accessible surface area. (d) Boxplots of active and inactive split sites. A two-sided Mann–Whitney  $U$  test was used for all properties but conservation and C-fragment docking for which a two-sided  $t$ -test was used. \*,  $p$ -value <0.05; \*\*,  $p$ -value <0.01; \*\*\*,  $p$ -value <0.001.

To evaluate the ability of each property to distinguish between active and inactive split sites, we calculated the *F*-value (Figure 3b), which is a metric that indicates how good the property is at correctly identifying active split sites, while minimizing mistakes. For the cases including additional residues beyond the split site itself, we calculated the *F*-value using the mean of the value of that specific property for different combinations of residues (Figure 3c). For 'conservation', we found that considering residues at positions 0, +1 and +3 gave the highest *F*-value (Figure 3c). Spatial conservation did not yield better results than sequence-based conservation (Figure S2; see Section 4 for the detailed explanation of how it was calculated). Therefore, the mean sequence-based conservation of residues at positions 0, +1 and +3 was finally used for this property. For 'relative surface area', residues -1 and +1 were used for the final property. For 'C-fragment docking', the highest *F*-value was obtained when including eight residues. All the tested properties were able to discriminate, in a statistically significant manner (Figure 3d), between active and inactive split sites, being, thus, promising for building the machine learning model.

## 2.3 | Generating the machine learning model

Once we identified several features that can individually distinguish active from inactive split sites, we needed to build the decision-making algorithm—the classifier—which leverages these features to make predictions on unseen data. For selecting the most suitable one for our specific purpose of active split site identification in inteins, we compared several classifiers (Gaussian Naive Bayes, XGBoost, Logistic Regression, Decision Tree, and Support Vector Machine) with all possible feature combinations based on their performance measured by a 10-fold cross validation (10 CV) of the Matthews correlation coefficient (MCC) averaged over 10 runs (10 × 10-fold cross validation) (Figure 4a, Figure S3). The logistic regression classifier operating on all the features (namely, sequence conservation, relative accessible surface area, binding affinity, C-fragment docking energy and secondary structure) performed best (average 10 × 10 cross-validated MCC of 0.55, with standard deviation of 0.02). Therefore, it was used to generate the final model (Figure 4b, Table S2).

With the training dataset, the model had an MCC of 0.57, an accuracy of 0.79 (10-fold cross-validated accuracy of  $0.784 \pm 0.118$ ), a precision of 0.79 and a recall of 0.77 (Figure 4c). The ROC (receiver operating characteristic) curve, which indicates the performance of a classification model at all classification thresholds in terms of true and

false positive rates, had an area under the curve of 0.84 (Figure 4d). The model was able to correctly predict 82%, 78% and 76% of the active split sites for *Npu* DnaE, gp41-1 and CL, respectively (Figure S4).

The model relies on a threshold to define a split site as active or inactive. Considering that the probability *p* is a value from 0 to 1, we set the default classification threshold at 0.5, so that any split site with a predicted probability  $p \geq 0.5$  is classified as active, while those with  $p < 0.5$  are classified as inactive. With this threshold, the true positive and negative rates are 0.79 and 0.78, respectively. The threshold can be, however, adjusted to specifically increase one of these rates, something that might be required in specific cases (Figure 4e). By employing two different classification thresholds, the true positive or true negative rate can be individually increased. As changing the classification threshold also reduces the number of predicted split sites, we set the limit for these thresholds so that the number of predicted split sites does not go below half of the total number of experimentally validated active/inactive sites. Setting the threshold to 0.6, the true positive rate can be increased from 0.79 to 0.83; setting it to 0.4, the true negative rate can be increased from 0.78 to 0.84. Using these two thresholds, we created four categories of prediction certainty: active split sites ( $p \geq 0.5$ ), inactive split sites ( $p < 0.5$ ), active with high probability ( $p \geq 0.6$ ), and inactive with high probability ( $p < 0.4$ ).

Next, we were interested in knowing whether the model could be used to differentiate split sites characterized by lower or higher splicing efficiency (Source Data, File S2). To this end, the probability of a site to be active, as outputted by the model, was plotted for three groups: inactive split sites, split sites with moderate splicing efficiency (<50% of the splicing efficiency) and split sites with high splicing efficiency ( $\geq 50\%$  of the splicing efficiency). We found a significant difference between inactive and moderate efficiency sites, as well as between moderate and high efficiency sites (Figure 4f).

## 2.4 | Model validation

To assess the performance of the model, we extracted from the literature a dataset of 97 split sites in inteins, of which 57 active and 40 inactive, from 41 different inteins (Aranko et al., 2014) (Table S3). We excluded *Pfu* RIR1-1 and *Pfu* RIR1-2, as they were split inside their homing endonuclease/stirrup domain, as well as gp41-1 and *Npu* DnaE, since they are already contained in the training dataset. Given the presence of different inteins in this dataset, we reasoned it was well suited to evaluate the generalizability of the model, which was obtained with data from three inteins. It is important to note that this

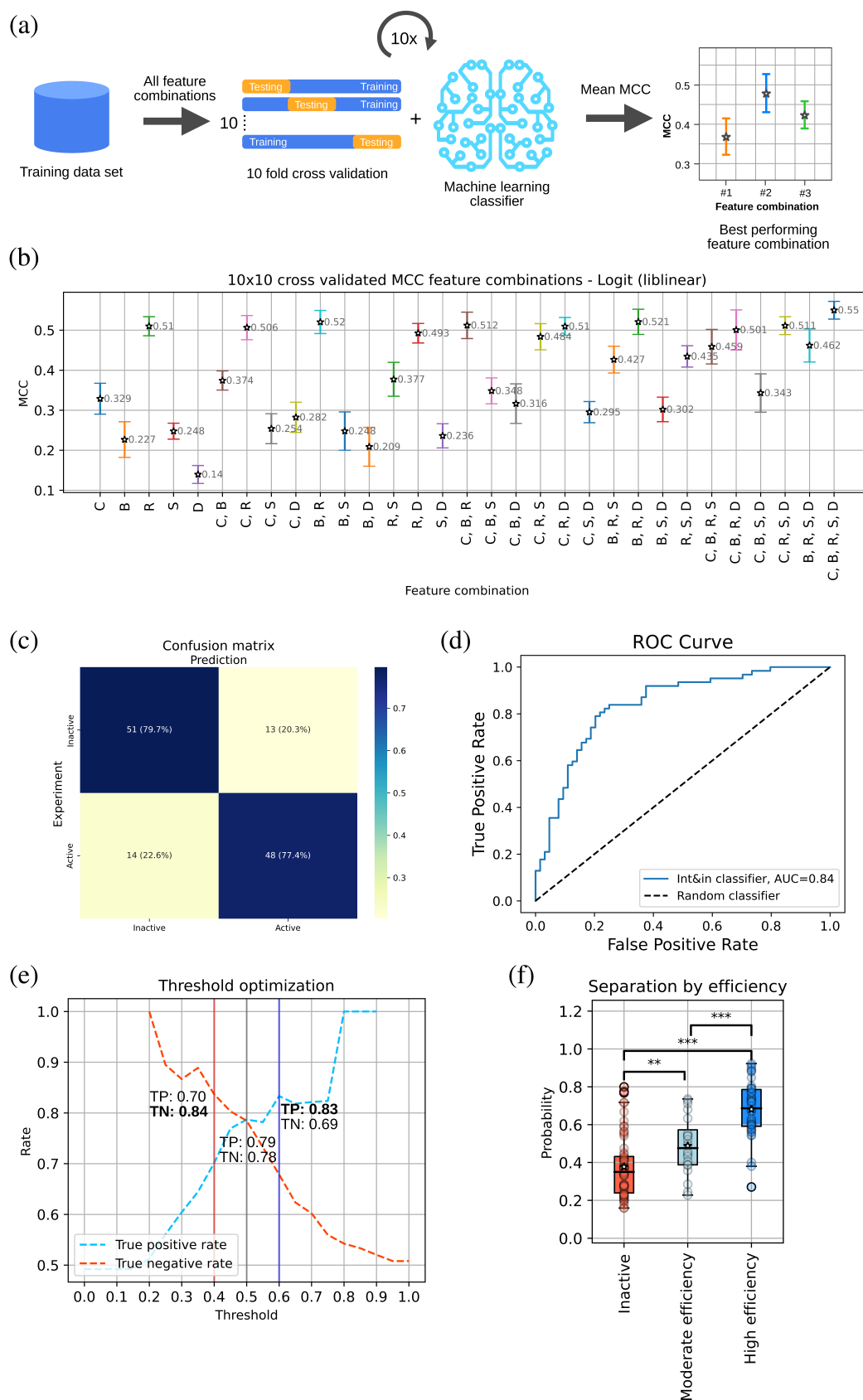


FIGURE 4 Legend on next page.

testing dataset, even though quite diverse from the point of view of the variety of inteins included, is unbalanced due to the prevalence of split sites clustering around the naturally occurring ones, as well as to the over-representation of active split sites (so-called class imbalance; 40 inactive vs. 57 active sites).

We generated the 3D structures of all the inteins with AlphaFold2 (Jumper et al., 2021) (implementation in ColabFold (Mirdita et al., 2022); *Source Data*, File S1), inputted them into the model, and then calculated performance measures (Figure 5a,b). We found an MCC of 0.55, an accuracy of 0.78 (10-fold cross-validated accuracy of  $0.732 \pm 0.152$ ), a precision of 0.76, a recall of 0.91 and a ROC of 0.83. Applying the same thresholds used with the training dataset, the true positive rate could be increased to 0.85 from 0.76, while the true negative rate decreased slightly from 0.83 to 0.82 (Figure 5c). The latter may be due to the imbalance of the dataset mentioned above.

To check for the effect of class imbalance, we employed an undersampling strategy based on the Near-Miss (version 3) technique (Lemaître et al., 2017), which selects samples from the majority class based on their closeness to samples in the minority class. Using this undersampled testing dataset, we obtained an MCC of 0.62, an accuracy of 0.79 (10-fold cross-validated accuracy of  $0.75 \pm 0.158$ ), a precision of 0.71, and a recall of 0.98 (Figure S5). Together, these results show that the logistic regression-based model performs similarly with the literature-derived validation dataset as with the training dataset containing sites spanning the whole sequence space of three inteins.

## 2.5 | The Int&in web server

To allow researchers of varying levels of computational knowledge to make use of this model, we opted for making it available through a freely-accessible web server

(<https://intein.biologie.uni-freiburg.de>), which is free of charge for academic usage. The Int&in web server evaluates each amino acid of a given intein sequence for its potential to be an active split site, and provides an easy-to-use web interface to quickly evaluate the results. Users can anonymously upload their experimentally determined or modeled protein structures and receive a personalized link to visualize the results. Additionally, we provide the option to submit batch runs with multiple .pdb files. Finally, users can register for an account, which ensures that past jobs are easily retrieved and can be analyzed at a later point (past jobs may be deleted after 30 days). After all calculations are executed on the backend, users are notified via email (if an address was provided at job submission; otherwise, the job can be accessed through the personalized link that appears after job submission), and can access an interface consisting of a structure window, a list of split sites and several graphs showing the values of the individual properties as well as the model predictions. All files generated by the Int&in web server as well as the raw data from third party programs (conservation calculations and secondary structure calculations) can be downloaded.

## 3 | DISCUSSION

Here we described Int&in, a web server that relies on a machine learning algorithm to predict active and inactive split sites in inteins. Before embarking in the development of this web server and the model it relies on, we checked the literature and found SPELL, a web server for the prediction of split sites in proteins specialized in the task of protein functional reconstitution by means of ligand- or light-regulated heterodimerizing systems (Dagliyan et al., 2018). Indeed, locating functional split sites in proteins is a highly desirable task, because splitting proteins into two dysfunctional halves, which can be brought back into close physical proximity to regain activity, is a useful technique in cell and

**FIGURE 4** Int&in machine learning model creation with the training dataset. (a) Illustration of the workflow for identifying the best feature combination and classifier. (b)  $10 \times 10$  CV MCCs plotted with their respective feature combinations. The following letters are used to code for the following features: C = conservation, B = binding affinity, R = relative accessible surface area, D = C-fragment docking, S = secondary structure. (c) Confusion matrix of the Int&in machine learning model based on the logistic regression classifier with the following features: conservation, relative accessible surface area and secondary structure. (d) ROC curve of the Int&in machine learning model compared to a random classifier. (e) Plot showing the probability threshold adjusted from 0 to 1 with increments of 0.05 plotted against the true positive and true negative. The respective rates of true positives are shown for three different thresholds: 0.4 (red), 0.5 (gray) and 0.6 (blue). (f) Plot showing the separation of the inteins according to different splicing efficiencies as predicted by the model. The inactive group shows no activity whatsoever ( $n = 64$ ), the moderate efficiency group contains all split sites leading to inteins with an activity  $<50\%$  ( $n = 20$ ) and the high efficiency group contains all split sites leading to inteins with an activity  $\geq 50\%$  ( $n = 42$ ). The two-sided Mann-Whitney  $U$  test was used for significance calculation, since the moderately efficient and highly efficient groups are not normally distributed. \*,  $p$ -value  $<0.05$ ; \*\*,  $p$ -value  $<0.01$ ; \*\*\*,  $p$ -value  $<0.001$ .



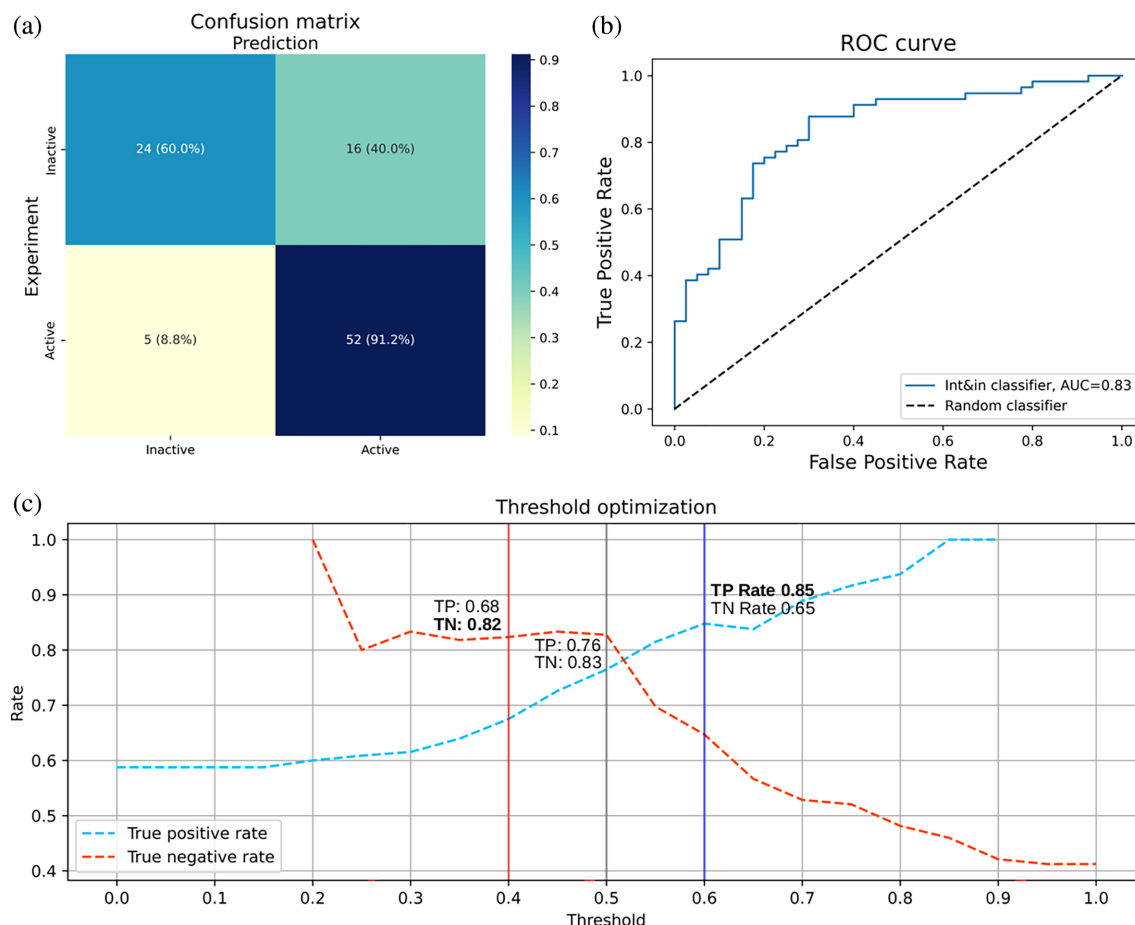


**FIGURE 5** Int&in performs well on a testing dataset. (a) Confusion matrix of the Int&in machine learning model with the dataset of split sites from literature. (b) ROC curve of the Int&in machine learning model compared to a random classifier. (c) Plot showing the probability threshold adjusted from 0 to 1 with increments of 0.05 plotted against the true positive and true negative rates. The rates are shown for three different thresholds: 0.4 (red), 0.5 (gray) and 0.6 (blue).

synthetic biology to control and/or understand biological processes (Cali & Brini, 2021; Mahameed et al., 2022; Varn-Buhler et al., 2022). The algorithm behind SPELL makes use of an energy function and several structural and sequence-based parameters to determine functional split sites. Because it was generated from a limited data set of 27 functional split sites from 16 different proteins, it is difficult to assess whether the rules employed by SPELL truly reflect the full range of sites at which a protein can be split. This was not the main goal of the SPELL algorithm, which aims to maximize the number of true positive sites while keeping the number of false positive sites at a minimum. This means that several functional split sites that are not deemed optimal by the algorithm are lost, which can be problematic when wishing to split a protein in a specific region. For inteins in particular, the possibility to find split sites in specific regions can be crucial to, for instance, generate very short intein fragments, which can be more easily chemically synthesized and used in protein semisynthesis (Ludwig et al., 2006; Mootz, 2009; Burton et al., 2020) or be more amenable to control via caging within the light-

sensitive light oxygen voltage (LOV) domain (Wong et al., 2015). Interestingly, when applied to 41 individual inteins, SPELL predicts no split sites for around 80% of the inteins tested (Table S1). Additionally, when we applied the same energy profile used by SPELL, which is conceptually equivalent to the binding energy we use, we found no significant difference between inactive and active split sites (Figure S6a,b). This indicates that SPELL is not particularly suitable to predict active split sites in inteins. Very recently, another algorithm, ProteinSplit, has been developed to specifically predict how to split a protein of interest for functional reconstitution via a ligand (Rihtar et al., 2023). Since this model requires a ligand, it is not immediately applicable to the vast majority of inteins, which spontaneously splice and are not ligand-dependent.

Our model uses binding affinity between the resulting intein fragments, as well as conservation, relative accessible surface area, C-fragment docking energy and secondary structures of and around the split site to calculate a probability score. Trained on randomly distributed split sites from three different inteins amounting to 126 sites

in total, the model achieved an accuracy of 0.78 with an untrained dataset consisting of 41 different inteins with split sites gathered from literature. Given their reliance on the training dataset to learn the patterns in the data, it is not surprising that machine learning algorithms strongly depend on the size of the training dataset, with larger ones leading to better predictive power (Sordo & Zeng, 2005). We were pleased to see that our model performs well despite the modest size of the training dataset.

As the model was not trained with any knowledge of the efficiency of splicing of each site, but nonetheless managed to output probabilities that show a significant difference between split sites associated with moderate and high splicing efficiencies, we speculate that the properties used in the model are also predictive of splicing efficiency associated with each split site, and thus Int&in could be used also to predict efficiencies. By testing the model on a dataset coming from the literature, characterized by a variety of inteins with different exteins expressed in different model organisms, we have shown generalizability as well as wide applicability of our model. Nonetheless, in cases where the local exteins are changed or truncated the model's output may show discrepancies, considering the model was trained on results generated with the optimal local exteins for each intein.

Additionally, we would like to encourage researchers to share the “negative data” (in the case of inteins, split sites that result in non-splicing inteins) as well, since such data would be equally informative as “positive data” and would prevent class imbalance issues in future ML algorithms' development. While the presence of class imbalance was not problematic for our particular application, it might be quite deleterious in others. In general, training ML models on diverse and large datasets would result in improved generalization, reduced overfitting, enhanced model complexity, improved accuracy and stability, better data representation and better learning performance.

The source code for a standalone version of the tool as well as the files for feature selection, model training and testing can be accessed at <https://github.com/bleblebles/Int-In/>. Since the Int&in web server is user-friendly, and requires no prior knowledge of bioinformatics or computational biology, we believe it will boost research on these fascinating proteins as well as applications based on them.

## 4 | MATERIALS AND METHODS

### 4.1 | Non-covalent bond determination in Int&in

A list of residues that are in proximity to each other (10 Å at most) is created and the existence of non-

covalent bonds (hydrogen bond, salt bridge, van der Waals, pi-pi and pi-cation) is determined, as outlined below.

### 4.2 | Hydrogen bonds

A hydrogen bond between two atoms is considered to be present if the angle between the hydrogen donor (D) and the hydrogen acceptor (A) is  $\leq 63^\circ$  and the distance between them is  $\leq 3.5$  Å (40). N, O, S and atoms may be acceptors and/or donors with the exception of  $\text{NH}_3$ , which cannot be an electron acceptor. Moreover, C atoms may be donors, to account for backbone hydrogen bonds (Gu et al., 1999). Donor atoms additionally need at least one hydrogen atom covalently bound to them.

### 4.3 | Salt bridges

A salt bridge between two residues is considered to be present if they have opposite charge and the distance between any of the nitrogen atoms in the side chain of the positively charged residue and the oxygen atoms (or the sulfur of cysteine) in the side chain of the negatively charged residue is  $\leq 4$  Å (Barlow & Thornton, 1983).

### 4.4 | Aromatic interactions

$\pi$ - $\pi$  interactions are attributed to aromatic amino acids if the centroids of their aromatic rings are at most 7.5 Å from each other and none or only one of the aromatic rings is positively charged (Bhattacharyya et al., 2002). Cation- $\pi$  interactions are considered to be present if the distance between the centroid of the aromatic ring of a neutral aromatic amino acid and any nitrogen atom of the side chain of a positively charged lysine or arginine is  $\leq 6$  Å (Gallivan & Dougherty, 1999).

### 4.5 | van der Waals

A van der Waals interaction is considered to be present between any carbon-carbon, carbon-sulfur, carbon-oxygen (glutamine OE1 and asparagine OD1) and carbon-nitrogen (glutamine NE2 and asparagine OE1) if their distance is  $\leq 0.5$  Å (Lovell et al., 1999). The van der Waals radii (NACCESS radii) of the two potentially interacting atoms is subtracted from the distance between the atoms to get the distance between the atoms' surfaces (Hubbard et al., 1993).

#### 4.6 | C-fragment docking energy determination in Int&in

The docking energy between the first eight residues of the C-intein and all residues of the N-intein is calculated by attributing different energies to each non-covalent interaction depending on its type (and distance, in the case of hydrogen bonds):

Non-covalent interaction	Energy (kJ/mol)
Hydrogen bond	For distances between D and A $\leq 1.5$ Å: 115.0 For distances between $1.5$ Å $< D$ and A $\leq 2.2$ Å: 40.0 For distances between $2.2$ Å $< D$ and A $\leq 3.5$ Å: 17.0
Salt bridge	20.0
Aromatic interaction	Pi-pi interaction: 9.4 Pi-cation interaction: 9.6
van der Waals	6.0

The energies have been used according to the RING 3.0 web server (Clementel et al., 2022).

#### 4.7 | Relative accessible surface area determination in Int&in

The accessible surface area of each residue is calculated with the 'rolling ball' algorithm by Shrake and Rupley (1973). The van der Waals radius as defined in NACCESS (Hubbard et al., 1993) is used, 100 sampling points are evenly placed on this sphere through the Fibonacci lattice method (Gonzalez, 2010) and a probe radius of 1.4 Å is used. To calculate the relative accessible surface area (RelASA) of a residue, the accessible surface of a residue (ASA) is divided by its maximum accessible surface (MaxASA) as defined in NACCESS (Hubbard et al., 1993):

$$\text{RelASA} = \frac{\text{ASA}}{\text{MaxASA}}$$

#### 4.8 | Conservation determination in Int&in

The conservation is calculated by first using HMMER (3.3) homologous sequences in the Uniref90 database (version 2021\_03) (Eddy, 1998; Suzek et al., 2015). Only entries with an *E*-value  $\leq 0.0001$ , an alignment length of

$\geq 70$  and a minimum of 35% sequence identity with the input sequence portion are kept to filter out false positives or too small sequences. If multiple domains are found, they are considered as unique hits and subjected to the same filters as described above. If there are more than 2000 sequences, due to technical limitations of the multiple sequence alignment software, these are sampled as follows: first, the number of total sequences is divided by 2000, then the resulting number is iteratively added to itself and the sums, rounded down, are used to sample the sequences. For instance, if 2500 sequences are found,  $2500/2000$  gives an interval of 1.25, leading to the following sequences being selected: 1, 2, 3, 4, 6, 7, 8, 9, 11,.... This procedure enables reproducible results while sampling through the whole HMMER output. The resulting sequences are then used to create a multiple sequence alignment (MSA) with the sequence in the .pdb file submitted by the user with the MUSCLE program (Edgar, 2004). The resulting MSA is then used to create clusters of sequences with  $\geq 95\%$  similarity (blank spaces in the MSA are not considered) between each other. One representative sequence out of each cluster is then taken for further evaluation. Due to program-related restrictions, the clusters are once again sampled according to the same principles described above to a maximum of 150 cluster sequences. For inteins, in most cases there are no more than 150 clusters, thus sampling does not occur. The clustered sequences are then passed to Rate4Site (Pupko et al., 2002; Mayrose et al., 2004), which calculates conservation scores. The conservation scores are then normalized to a scale of 0 and 1 according to the following formulas, similarly to how the bins are created in the ConSurf web-server (Ashkenazy et al., 2016):

$$\text{NormCons} = \left( 1 - \frac{\text{Cons} - \text{PositiveCons}_{\min}}{\text{PositiveCons}_{\max} - \text{PositiveCons}_{\min}} \right) \times 0.5$$

for sites that have a positive conservation (non-conserved sites), with NormCons being the normalized conservation, Cons being the current residues' conservation,  $\text{PositiveCons}_{\min}$  being the minimal positive conservation out of all residues, and  $\text{PositiveCons}_{\max}$  being the maximal positive conservation of all residues and

$$\text{NormCons} = \left( 1 - \frac{\text{Cons} - \text{NegativeCons}_{\min}}{\text{NegativeCons}_{\max} - \text{NegativeCons}_{\min}} \right) \times 0.5 + 0.5$$

for sites that have a negative conservation (conserved sites), with NormCons being the normalized conservation, Cons being the current residues' conservation,  $\text{NegativeCons}_{\min}$  being the minimal negative conservation out of all residues, and

NegativeCons<sub>max</sub> being the maximal negative conservation of all residues.

## 4.9 | Spatial conservation determination

Spatial conservation was calculated based on mean, minimum and maximum conservation values of all residues that have a specified maximum distance from the split site. For this, C $\alpha$ -atom positions were used, while the split site position was denoted as the middle of C $\alpha$ -atom positions of the two flanking residues at the split site.

## 4.10 | Binding affinity determination in Int&in

The binding affinity between two fragments is calculated through the PRODIGY prediction model established by Vangone and Bonvin (2015, 2017). The model is implemented in the backend of the Int&in web server by refactoring the code from Python to C#. The surface accessibility is calculated through an implementation of the algorithm by Lee and Richards (1971) and Mitternacht (2016) as outlined in the FreeSASA source code, with 20 sphere slices and the van der Waals radii and maximally accessible surface areas as defined by the NACCESS program (Hubbard et al., 1993).

## 4.11 | Secondary structure determination in Int&in

The secondary structure of a sequence is calculated with the DSSP program (Kabsch & Sander, 1983; Joosten et al., 2011). A split site is considered to be in a secondary structure if both flanking residues are part of a secondary structure.

## 4.12 | Computational resources needed for Int&in

The Int&in web server consists of two distinct parts: a backend written in C# (.Net 3.1) and Python 3 performing the calculations, and a web GUI written in PHP and JavaScript. After submitting a file, the file is stored for at least 30 days on the server and is accessible through a personalized unique key. The file as well as the user options are passed from the web GUI to the backend to perform the calculations. The current job status can be accessed through the personalized unique key given to the user. If the user provided an email at submission, a notification

will be sent when the job has finished. Otherwise, they will have to check the personalized link to see if the job has finished. The backend makes use of the following libraries: DotNetZip (<https://github.com/haf/DotNetZip.Semverd>), MailKit (<https://github.com/jstedfast/MailKit>) and MimeKit (<https://github.com/jstedfast/MimeKit>). Additionally, the following programs are used for the indicated tasks:

- PDB2PQR v2.1.1—to generate the structure at a pH of 7 and to add hydrogens
- DSSP (3.0.0)—to generate the secondary structure
- HMMER (3.3)—to identify homologous proteins in the UniRef90 database (2021\_03)
- Muscle (v3.8.1551)—to create a multiple sequence alignment (MSA) of the sequence contained in the .pdb file submitted by the user and maximum 2000 sequences extracted from the HMMER output
- Rate4Site (3.0.0.)—to generate the conservation score out of maximum 150 clustered sequences from the MSA
- Python, with the following two libraries: scikit-learn (1.1.0) and pandas.

The web-based GUI makes use of the following JavaScript libraries: jQuery (<https://github.com/jquery/jquery>), NGL viewer for molecular representation (Rose & Hildebrand, 2015) and dygraphs for chart plots (<https://github.com/danvk/dygraphs>). The web-based GUI also lets the user create an account to have an overview of the submitted jobs. The account information is stored in a MySQL database. Passwords are hashed for security.

## 4.13 | Property significance tests

To assess if the difference between the group of split sites predicted to be active and that of split sites predicted to be inactive was significant when using a defined property, we applied either the *t*-test or the Mann–Whitney *U* test (scipy.stats.ttest\_ind, mannwhitneyu), depending on whether the groups were considered normally distributed or not, respectively. Normal distribution was evaluated using the Shapiro–Wilk test, the normaltest function from scipy and the Anderson–Darling test (scipy.stats.shapiro, normaltest, anderson).

## 4.14 | Property optimization with ANOVA *F*-scores

The ANOVA *F*-scores were calculated with the sklearn library in Python.

(sklearn.feature\_selection.SelectKBest, f\_classif ).



#### 4.15 | Feature combination selection

Different combinations of features were evaluated on different models (from `sklearn.naive_bayes.GaussianNB`, `xgboost.XGBClassifier`, `sklearn.linear_model.LogisticRegression`, `sklearn.tree.DecisionTreeClassifier`, and `sklearn.svm.SVC`) by calculating the 10x Cross-validated (sklearn.model\_selection.KFold with shuffle set to true) Matthews correlation coefficient (MCC, `sklearn.metrics.matthews_corrcoef`), which was then averaged over 10 runs with different seeds (from `numpy.random.seed`, seeds 0–9 were used).

#### 4.16 | Model creation

The logistic regression model (from `sklearn.linear_model.LogisticRegression` (Pedregosa et al., 2011); with the ‘liblinear’ solver, which was selected due to the smaller dataset), was trained in Python on the training dataset. To evaluate the model in terms of accuracy, precision, recall, and MCC confusion matrices were generated (`sklearn.metrics.accuracy_score`, `precision_score`, `recall_score`, `matthews_corrcoef`, `confusion_matrix`). The confusion matrix representation was generated through `seaborn` (Waskom, 2021). The model was saved through the pickle library in Python.

#### 4.17 | Protein structures

The crystal structures of gp41-1 and *Npu* DnaE (PDB id: 6QAZ and PDB id: 4KL5, respectively) were used. The structures were additionally modified in PyMol to remove any extein sequences and mutate residues so that they would represent the native structures. For the gp41-1 intein structure, the first three extein residues (SGG) were removed and the fourth alanine (which inactivates the intein) was mutated back to cysteine. For *Npu* DnaE chain A was used for the computational experiments and the first three extein residues were also removed and the fourth alanine residue was mutated to cysteine; additionally, the last four extein residues (ADNG) in the structure file were also removed. CL as well as all other inteins from the literature data set were modeled through the ColabFold implementation (Mirdita et al., 2022) of AlphaFold2 (Jumper et al., 2021).

#### 4.18 | Plasmid construction

For the expression of all intein constructs in *E. coli*, the pTrc99A vector was used. A list of all used primers and

amino acid sequences of exemplary plasmids is given in the Appendix, File S5. For PCR amplification the Phusion Flash High-Fidelity PCR Master Mix (2×) from Thermo-Scientific and the Biometra TOne 96G thermocycler from Analytik Jena were used. Plasmids were constructed using the NEBuilder® HiFi DNA Assembly Cloning Kit from New England Biolabs.

The *mbp* gene coding for the maltose binding protein (MBP) was amplified from pETM41 via PCR with primers pTrc\_MBP\_fw and MBP\_gp41\_rev (Figure S7a, upper left panel). Note that the gene in the final plasmids contains a mutation in the first base of the second codon, which means that the protein has lysine instead of glutamic acid at that position. Since the anti-MBP antibody worked well we decided against removing the mutation. The *trx* gene coding for thioredoxin (TRX) was amplified from pETTrx with primers TRX\_fw and TRX\_SUMO\_rev (Figure S7a, upper middle panel). Plasmids pETM41 and pETTrx were a kind gift of Gunter Stier (Heidelberg University). The *Saccharomyces cerevisiae smt3* gene coding for SUMO was amplified from pTB324\_AmiB (kind gift of Thomas Bernhardt, Harvard Medical School, Boston) with primers SUMO\_fw and SUMO\_rev (Figure S7a, upper right panel). The N- and C-fragments of the *gp41-1* gene were amplified with primers gp41-1\_fw and gp41-1\_N\_merge\_rev, and primers gp41-1\_rev and gp41-1\_C\_merge\_fw, respectively, from pSiMPlk (Palanisamy et al., 2019) (Figure S7a, lower left panel). The backbone fragments were amplified with primers pTrc\_BB\_rev and CoLE1\_fw as well as CoLE1\_rev and SUMO\_BB\_fw from pTrc99A in order to have shorter fragments. All fragments (backbone 1, backbone 2, mbp, gp41-1 N-fragment, gp41-1 C-fragment, trx, sumo; Figure S7b, upper panel) contain overhangs allowing for assembly yielding pTRC-MBP-gp41-1-TRX-GS-SUMO-FLAG (Figure S7b, lower left panel). Subsequently, GS linkers (one GS linker consists of the following sequence: GGGGSGGGGS) were added upstream of the local exteins of the N-intein and downstream of the local exteins of the C-intein (Figure 2c) in pTRC-MBP-gp41-1-TRX-GS-SUMO-FLAG plasmid with primers MBP\_GS\_rev and CoLE1\_fw, Intein\_GS\_TRX\_fw and CoLE1\_rev as well as GP41\_GS\_Nextein\_fw and GP41\_Cextein\_rev yielding pTRC-MBP-GS-gp41-1-GS-TRX-GS-SUMO-FLAG (Figure S7b, lower right panel). pTRC-MBP-GS-GS-TRX-GS-SUMO-FLAG containing the N- and C-exteins and the native local extein sequences for gp41-1 (positive control) was generated from pTRC-MBP-GS-gp41-1-GS-TRX-GS-SUMO-FLAG using primers GS\_GP\_N\_and\_C\_Ext\_fw, CoLE1\_rev and GS\_Next\_rev and CoLE1\_fw.

The constructs with *Npu* DnaE and CL were constructed using pTRC-MBP-gp41-1-TRX-GS-SUMO-FLAG as template. The gene coding for full-length *Npu* DnaE

was amplified with primers MBP\_GS\_rev and CoLE1\_fw, Intein\_GS\_SUMO\_fw and CoLE1\_rev as well as *Npu*\_CExtein\_rev and *Npu*\_NExtein\_fw yielding pTRC-MBP-GS-*Npu*\_DnaE-GS-TRX-GS-SUMO-FLAG. The gene coding for CL was amplified from pTT32 and pTT43 (kind gift of Henning Mootz, University of Münster; Bhagawati et al., 2019). Specifically, the N-intein was amplified from pTT32 with primers AesN\_GS\_fw and AesN\_rev, while the C-intein was amplified from pTT43 with primers AesC\_fw and AesC\_GS\_rev. The two backbone fragments were amplified from pTRC-MBP-GS-gp41-1-GS-TRX-GS-SUMO-FLAG with primers MBP\_GS\_rev and CoLE1\_fw, Intein\_GS\_SUMO\_fw and CoLE1\_rev. The four fragments were then assembled into pTRC-MBP-GS-CSIntein-GS-TRX-GS-SUMO-FLAG.

To clone the different split sites, we generated a so-called 'split cassette', containing a stop codon, a frame-shifted stop codon followed by a random spacer DNA, a ribosome binding site (Elowitz & Leibler, 2000) and a start codon. This split cassette was inserted in the intein-containing plasmid via two overlapping primers encoding the split cassette in their overhangs and annealing to the sequence of the intein at the respective split site (see *Source Data*, File S5 for a list of representative and unique plasmid sequences and a full list of primers. The split cassette primers contain the name of the respective intein and the split site). Two primers annealing to the backbone (CoLE1\_fw and CoLE1\_rev) were used to generate two fragments with the primers containing the split cassette. Note that all constructs contain the same exteins and the same flexible linkers (GGGGSGGGGS) that separate them from the local exteins. The only difference among constructs is the local exteins, which are specific to the intein (Figure 2c).

#### 4.19 | Bacterial cell lysis

Individual colonies were picked and used to start overnight (ON) cultures, which were grown at 37°C with 250 rpm shaking in the multitron pro incubator (Infors AG). The next morning, a volume of  $(100/\text{OD}) \times 3 \mu\text{L}$  of the ON culture was used to inoculate a fresh tube with 3 mL LB medium plus ampicillin (100 mg/L). The tubes were subsequently shaken at 37°C and 250 rpm for 90 min, after which 3  $\mu\text{L}$  of 1 M Isopropyl  $\beta$ -D-1-thiogalactopyranoside (IPTG) were added to each tube. The tubes were then put again inside the incubator and shook for 2 h and 30 min at 37°C 250 rpm. Afterwards, the OD600 of each culture was measured and a volume of  $100/\text{OD} \mu\text{L}$  was taken and centrifuged at 13,000 rpm for 4 min at room temperature. The supernatant was removed from the samples, and the pellets resuspended in 20  $\mu\text{L}$  4 $\times$  Lämmli Buffer (Bio-Rad) and 80  $\mu\text{L}$

ddH<sub>2</sub>O. The tubes were heated up for 10 min at 95°C and stored at –20°C. The OD at 600 nm of the bacterial cultures was measured with the OD600 DiluPhotometer from IMPLIN GmbH.

#### 4.20 | Western blot

1.5  $\mu\text{L}$  of each cell extract were loaded in a well of a Mini-PROTEAN® 10% TGX™ Precast Gel (10 wells, 50  $\mu\text{L}$  pocket volume; Bio-Rad) and separated in the Mini-PROTEAN Tetra Vertical Electrophoresis Cell (Bio-Rad) at 100 V for around 1 h and 30 min. Protein transfer onto a PVDF membrane was carried out with the Trans-Blot Turbo Mini 0.2  $\mu\text{m}$  PVDF Transfer Packs (Bio-Rad) and Trans-Blot Turbo Transfer System (Bio-Rad). The membrane was blocked for 2 h with 5% BSA-PBST solution at room temperature on a rocking machine at 25 rpm. The blocking buffer was removed and 10 mL 5% BSA-PBST with 1  $\mu\text{L}$  RABBIT anti-DYKDDDDK Tag antibody (Bio-Rad, # AHP1074), 1  $\mu\text{L}$  anti-MBP monoclonal antibody (New England Biolabs, #E8032L) and 6  $\mu\text{L}$  anti-*E. coli* RNA Polymerase  $\beta$ -subunit antibody (BioLegend, #663905) were added. The membrane was then placed on a rocking machine at 25 rpm for another 2 h. The BSA-PBST antibody mixture was then removed and the membrane was washed three times with PBST with gentle rocking for 5 min. 4  $\mu\text{L}$  of the Cy5 goat anti-rabbit antibody (Invitrogen, #A10523) and 4  $\mu\text{L}$  of the Alexa Fluor goat anti-mouse antibody (Invitrogen, #A11029) were added to 10 mL BSA-PBST and poured over the membrane in a closed box (used to protect it from light). The box containing the membrane was placed on the rocking machine at 25 rpm for another hour. Subsequently, the secondary antibody mixture was removed followed by three washes with PBST, during which the membrane was rocked for 5 min in the dark box. The membranes were imaged with the Amersham Typhoon 5 (Global Life Sciences Solutions) with the Cy2 and Cy5 emission filters and excitation wavelengths.

#### 4.21 | Calculation of splicing efficiencies

Image J2 (1.53 s) (Rueden, 2017) was used to calculate the efficiency of splicing for each split site according to the following formula:

$$\text{Efficiency} = \frac{\text{Area}_{\text{spliceproduct}}}{\text{Area}_{\text{spliceproduct}} + \text{Area}_{\text{precursor}}}$$

The efficiencies were calculated for both channels (one channel detects the C-extein and one the N-extein). The maximum value was used to train the model.

## 4.22 | Definition of experimentally validated active split site

Two independent WBs were performed for each split site for each tested intein. A split site was considered active only if the splice product was quantifiable in both replicates.

### AUTHOR CONTRIBUTIONS

**Mirko Schmitz:** Methodology; software; writing – original draft; formal analysis; data curation; investigation; validation; visualization. **Jara Ballestin Ballestin:** Validation; methodology; data curation. **Junsheng Liang:** Methodology; validation; data curation. **Franziska Tomas:** Methodology; validation; data curation. **Leon Freist:** Software. **Karsten Voigt:** Software. **Barbara Di Ventura:** Writing – review and editing; supervision; funding acquisition; resources; formal analysis. **Mehmet Ali Öztürk:** Conceptualization; supervision; formal analysis.

### ACKNOWLEDGMENTS

This work was supported by the European Research Council (ERC) under the European Union's Horizon 2020 research and innovation program (grant agreement no. 101002044 to BDV), and partly by the Deutsche Forschungsgemeinschaft (DFG, German Research Foundation)—Project #422681845 within SFB1425. Open Access funding enabled and organized by Projekt DEAL.

### CONFLICT OF INTEREST STATEMENT

The authors declare that there are no competing interests.

### ORCID

Mirko Schmitz  <https://orcid.org/0009-0005-9379-6590>

Barbara Di Ventura  <https://orcid.org/0000-0002-0247-9989>

Mehmet Ali Öztürk  <https://orcid.org/0000-0002-0840-1402>

### REFERENCES

- Appleby JH, Zhou K, Volkmann G, Liu XQ. Novel split intein for trans-splicing synthetic peptide onto C terminus of protein. *J Biol Chem*. 2009;284:6194–9.
- Aranko AS, Wlodawer A, Iwai H. Nature's recipe for splitting inteins. *Protein Eng Sel*. 2014;27:263–71.
- Ashkenazy H, Abadi S, Martz E, Chay O, Mayrose I, Pupko T, et al. ConSurf 2016: an improved methodology to estimate and visualize evolutionary conservation in macromolecules. *Nucleic Acids Res*. 2016;44(W1):W344–50.
- Barlow DJ, Thornton JM. Ion-pairs in proteins. *J Mol Biol*. 1983; 168:867–85.
- Bhagawati M, Terhorst TME, Füsser F, Hoffmann S, Pasch T, Pietrovski S, et al. A mesophilic cysteine-less split intein for

- protein trans-splicing applications under oxidizing conditions. *Proc Natl Acad Sci*. 2019;116(44):22164–72.
- Bhattacharyya R, Samanta U, Chakrabarti P. Aromatic-aromatic interactions in and around alpha-helices. *Protein Eng*. 2002;15: 91–100.
- Böcker JK, Dörner W, Mootz HD. Rational design of an improved photo-activatable intein for the production of head-to-tail cyclized peptides. *Biol Chem*. 2019;400(3):417–27.
- Brenzel S, Kurpiers T, Mootz HD. Engineering artificially split inteins for applications in protein chemistry: biochemical characterization of the split Ssp DnaB intein and comparison to the split Sce VMA intein. *Biochemistry*. 2006;45:1571–8.
- Burton AJ, Haugbro M, Parisi E, Muir TW. Live-cell protein engineering with an ultra-short split intein. *Proc Natl Acad Sci U A*. 2020;117:12041–9.
- Cali T, Brini M. Quantification of organelle contact sites by split-GFP-based contact site sensors (SPLICS) in living cells. *Nat Protoc*. 2021;16:5287–308.
- Carvajal-Vallejos P, Pallisse R, Mootz HD, Schmidt SR. Unprecedented rates and efficiencies revealed for new natural split inteins from metagenomic sources. *J Biol Chem*. 2012;287: 28686–96.
- Choi H, Eom S, Kim H-U, Bae Y, Jung HS, Kang S. Load and display: engineering encapsulin as a modular nanoplatfor for protein-cargo encapsulation and protein-ligand decoration using Split Intein and SpyTag/SpyCatcher. *Biomacromolecules*. 2021;22(7):3028–39.
- Clementel D, Del Conte A, Monzon AM, Camagni GF, Minervini G, Piovesan D, et al. RING 3.0: fast generation of probabilistic residue interaction networks from structural ensembles. *Nucleic Acids Res*. 2022;50(W1):W651–6.
- Dagliyan O, Krokhotin A, Ozkan-Dagliyan I, Deiters A, Der CJ, Hahn KM, et al. Computational design of chemogenetic and optogenetic split proteins. *Nat Commun*. 2018;9(1):4042.
- Di Ventura B, Mootz HD. Switchable inteins for conditional protein splicing. *Biol Chem*. 2019;400(4):467–75.
- Eddy SR. Profile hidden Markov models. *Bioinformatics*. 1998;14: 755–63.
- Edgar RC. MUSCLE: multiple sequence alignment with high accuracy and high throughput. *Nucleic Acids Res*. 2004;32:1792–7.
- Elowitz MB, Leibler S. A synthetic oscillatory network of transcriptional regulators. *Nature*. 2000;403:335–8.
- Ferruz N, Schmidt S, Höcker B. ProtGPT2 is a deep unsupervised language model for protein design. *Nat Commun*. 2022;13(1): 4348.
- Gallivan JP, Dougherty DA. Cation-pi interactions in structural biology. *Proc Natl Acad Sci U A*. 1999;96:9459–64.
- Gonzalez A. Measurement of areas on a sphere using fibonacci and latitude-longitude lattices. *Math Geosci*. 2010;42:49–64.
- Gu Y, Kar T, Scheiner S. Fundamental properties of the CH...O interaction: is it a true hydrogen bond? *J Am Chem Soc*. 1999; 121:9411–22.
- Hubbard S, Thornton J, N.A.C.C.E.S.S. Computer program. Dep. Biochem. Mol. Biol. University College, London; 1993.
- Iwai H, Zuger S, Jin J, Tam PH. Highly efficient protein trans-splicing by a naturally split DnaE intein from *Nostoc punctiforme*. *FEBS Lett*. 2006;580:1853–8.
- Joosten RP, te Beek TAH, Krieger E, Hekkelman ML, Hooft RWW, Schneider R, et al. A series of PDB related databases for everyday needs. *Nucleic Acids Res*. 2011;39:D411–9.

- Jovel J, Greiner R. An introduction to machine learning approaches for biomedical research. *Front Med*. 2021;8:771607.
- Jumper J, Evans R, Pritzel A, Green T, Figurnov M, Ronneberger O, et al. Highly accurate protein structure prediction with AlphaFold. *Nature*. 2021;596(7873):583–9.
- Kabsch W, Sander C. Dictionary of protein secondary structure: pattern recognition of hydrogen-bonded and geometrical features. *Biopolymers*. 1983;22:2577–637.
- Khakzad H, Igashov I, Schneuing A, Goverde C, Bronstein M, Correia B. A new age in protein design empowered by deep learning. *Cell Syst*. 2023;14(11):925–39.
- Khurana S, Rawi R, Kunji K, Chuang G-Y, Bensmail H, Mall R. DeepSol: a deep learning framework for sequence-based protein solubility prediction. *Bioinformatics*. 2018;34(15):2605–13.
- Kouba P, Kohout P, Haddadi F, Bushuiev A, Samusevich R, Sedlar J, et al. Machine learning-guided protein engineering. *ACS Catal*. 2023;13(21):13863–95.
- Lee G, Muir TW. Distinct phases of cellular signaling revealed by time-resolved protein synthesis. *bioRxiv*. 2023.
- Lee B, Richards FM. The interpretation of protein structures: estimation of static accessibility. *J Mol Biol*. 1971;55:379–400.
- Lemaître G, Nogueira F, Aridas CK. Imbalanced-learn: a python toolbox to tackle the curse of imbalanced datasets in machine learning. *J Mach Learn Res*. 2017;18(17):1–5.
- Lockless SW, Muir TW. Traceless protein splicing utilizing evolved split inteins. *Proc Natl Acad Sci U S A*. 2009;106(27):10999–1004.
- Lopez-Igual R, Bernal-Bayard J, Rodriguez-Paton A, Ghigo JM, Mazel D. Engineered toxin-intein antimicrobials can selectively target and kill antibiotic-resistant bacteria in mixed populations. *Nat Biotechnol*. 2019;37:755–60.
- Lovell SC, Word JM, Richardson JS, Richardson DC. Asparagine and glutamine rotamers: B-factor cutoff and correction of amide flips yield distinct clustering. *Proc Natl Acad Sci U A*. 1999;96:400–5.
- Ludwig C, Pfeiff M, Linne U, Mootz HD. Ligation of a synthetic peptide to the N terminus of a recombinant protein using semi-synthetic protein trans-splicing. *Angew Chem Int Ed Engl*. 2006;45:5218–21.
- Mahameed M, Wang P, Xue S, Fussenegger M. Engineering receptors in the secretory pathway for orthogonal signalling control. *Nat Commun*. 2022;13:7350.
- Mayrose I, Graur D, Ben-Tal N, Pupko T. Comparison of site-specific rate-inference methods for protein sequences: empirical Bayesian methods are superior. *Mol Biol Evol*. 2004;21:1781–91.
- Mirdita M, Schütze K, Moriwaki Y, Heo L, Ovchinnikov S, Steinegger M. ColabFold: making protein folding accessible to all. *Nat Methods*. 2022;19(6):679–82.
- Mitternacht S. FreeSASA: an open source C library for solvent accessible surface area calculations. *F1000Res*. 2016;5:189.
- Mootz HD. Split inteins as versatile tools for protein semisynthesis. *Chembiochem*. 2009;10:2579–89.
- Mootz HD, Blum ES, Tyszkiewicz AB, Muir TW. Conditional protein splicing: a new tool to control protein structure and function in vitro and in vivo. *J Am Chem Soc*. 2003;125(35):10561–9.
- Mootz HD, Muir TW. Protein splicing triggered by a small molecule. *J Am Chem Soc*. 2002;124:9044–5.
- Otomo T, Ito N, Kyogoku Y, Yamazaki T. NMR observation of selected segments in a larger protein: central-segment isotope labeling through intein-mediated ligation. *Biochemistry*. 1999;38:16040–4.
- Palanisamy N, Degen A, Morath A, Ballestin Ballestin J, Juraske C, Öztürk MA, et al. Split intein-mediated selection of cells containing two plasmids using a single antibiotic. *Nat Commun*. 2019;10(1):4967.
- Palei S, Becher KS, Nienberg C, Jose J, Mootz HD. Bacterial cell-surface display of semisynthetic cyclic peptides. *Chembiochem*. 2019;20:72–7.
- Pan D, Xuan B, Sun Y, Huang S, Xie M, Bai Y, et al. An intein-mediated modulation of protein stability system and its application to study human cytomegalovirus essential gene function. *Sci Rep*. 2016;6:26167.
- Pedregosa F, Varoquaux G, Gramfort A, Michel V, Thirion B, Grisel O, et al. Scikit-learn: machine learning in python. *J Mach Learn Res*. 2011;12(85):2825–30.
- Pupko T, Bell RE, Mayrose I, Glaser F, Ben-Tal N. Rate4Site: an algorithmic tool for the identification of functional regions in proteins by surface mapping of evolutionary determinants within their homologues. *Bioinformatics*. 2002;18(Suppl 1):71–7.
- Purde V, Kudryashova E, Heisler DB, Shakya R, Kudryashov DS. Intein-mediated cytoplasmic reconstitution of a split toxin enables selective cell ablation in mixed populations and tumor xenografts. *Proc Natl Acad Sci U A*. 2020;117:22090–100.
- Rihtar E, Lebar T, Lainšček D, Kores K, Lešnik S, Bren U, et al. Chemically inducible split protein regulators for mammalian cells. *Nat Chem Biol*. 2023;19(1):64–71.
- Rose AS, Hildebrand PW. NGL viewer: a web application for molecular visualization. *Nucleic Acids Res*. 2015;43(W1):W576–9.
- Rueden CT. ImageJ2: ImageJ for the next generation of scientific image data. *BMC Bioinformatics*. 2017;18:529.
- Shah NH, Eryilmaz E, Cowburn D, Muir TW. Naturally split inteins assemble through a “capture and collapse”. *Mech J Am Chem Soc*. 2013;135:18673–81.
- Shah NH, Muir TW. Inteins: nature's gift to protein chemists. *Chem. Sci*. 2013;5(2):446–61.
- Shrake A, Rupley JA. Environment and exposure to solvent of protein atoms. *Lysozyme Insul J Mol Biol*. 1973;79:351–71.
- Sordo M, Zeng Q. On sample size and classification accuracy: a performance comparison. In: Oliveira JL, Maojo V, Martín-Sánchez F, Pereira AS, editors. *Biological and medical data analysis*. Berlin, Heidelberg: Springer; 2005. p. 193–201.
- Stevens AJ, Sekar G, Shah NH, Mostafavi AZ, Cowburn D, Muir TW. A promiscuous split intein with expanded protein engineering applications. *Proc Natl Acad Sci*. 2017;114(32):8538–43.
- Suzek BE, Wang Y, Huang H, McGarvey PB, Wu CH, UniProt Consortium. UniRef clusters: a comprehensive and scalable alternative for improving sequence similarity searches. *Bioinforma Oxf Engl*. 2015;31(6):926–32.
- Tyszkiewicz AB, Muir TW. Activation of protein splicing with light in yeast. *Nat Methods*. 2008;5:303–5.
- Vangone A, Bonvin AM. Contacts-based prediction of binding affinity in protein-protein complexes. *Elife*. 2015;4:7454.
- Vangone A, Bonvin A. PRODIGY: a contact-based predictor of binding affinity in protein-protein complexes. *Biol Protocol*. 2017;7:2124.
- VarnBuhler BS, Moon J, Dey SK, Wu J, Jaffrey SR. Detection of SARS-CoV-2 RNA using a DNA aptamer mimic of green fluorescent protein. *ACS Chem Biol*. 2022;17:840–53.



- Villalobos-Alva J, Ochoa-Toledo L, Villalobos-Alva MJ, Aliseda A, Pérez-Escamirosa F, Altamirano-Bustamante NF, et al. Protein science meets artificial intelligence: a systematic review and a biochemical meta-analysis of an inter-field. *Front Bioeng Biotechnol*. 2022;10:788300.
- Villiger L, Grisch-Chan HM, Lindsay H, Ringnalda F, Pogliano CB, Allegri G, et al. Treatment of a metabolic liver disease by in vivo genome base editing in adult mice. *Nat Med*. 2018;24(10):1519–25.
- Waldhauer MC, Schmitz SN, Ahlmann-Eltze C, Gleixner JG, Schmelas CC, Huhn AG, et al. Backbone circularization of *Bacillus subtilis* family 11 xylanase increases its thermostability and its resistance against aggregation. *Mol Biosyst*. 2015;11(12):3231–43.
- Wang J, Han L, Chen J, Xie Y, Jiang H, Zhu J. Reduction of non-specific toxicity of immunotoxin by intein mediated reconstitution on target cells. *Int Immunopharmacol*. 2019;66:288–95.
- Wang Y, Mei C, Zhou Y, Wang Y, Zheng C, Zhen X, et al. Semi-supervised prediction of protein interaction sites from unlabeled sample information. *BMC Bioinformatics*. 2019;20(25):699.
- Wang Y, Tang H, Huang L, Pan L, Yang L, Yang H, et al. Self-play reinforcement learning guides protein engineering. *Nat Mach Intell*. 2023;5(8):845–60.
- Waskom ML. seaborn: statistical data visualization. *J Open Source Softw*. 2021;6(60):3021.
- Watson JL, Juergens D, Bennett NR, Trippe BL, Yim J, Eisenach HE, et al. De novo design of protein structure and function with RFdiffusion. *Nature*. 2023;620(7976):1089–100.
- Wong S, Mosabbir AA, Truong K. An engineered Split Intein for photoactivated protein trans-splicing. *PLoS One*. 2015;10:135965.
- Wu H, Xu MQ, Liu XQ. Protein trans-splicing and functional mini-inteins of a cyanobacterial dnaB intein. *Biochim Biophys Acta*. 1998;1387:422–32.
- Yao Z, Aboualizadeh F, Kroll J, Akula I, Snider J, Lyakisheva A, et al. Split Intein-mediated protein ligation for detecting protein-protein interactions and their inhibition. *Nat Commun*. 2020;11(1):2440.
- Ye B, Shen W, Shi M, Zhang Y, Xu C, Zhao Z. Intein-mediated backbone cyclization of entolimod confers enhanced radioprotective activity in mouse models. *PeerJ*. 2018;6:e5043.

## SUPPORTING INFORMATION

Additional supporting information can be found online in the Supporting Information section at the end of this article.

**How to cite this article:** Schmitz M, Ballestin JB, Liang J, Tomas F, Freist L, Voigt K, et al. Int&in: A machine learning-based web server for active split site identification in inteins. *Protein Science*. 2024; 33(6):e4985. <https://doi.org/10.1002/pro.4985>